Plasma rotation in a plasma generator

H. Meyer,* S. Klose, E. Pasch,† and G. Fussmann
Bereich Plasmadiagnostik, Max-Planck-Institut für Plasmaphysik, Mohrenstrasse 41, D-10117 Berlin, Germany
(Received 17 September 1999)

The plasma rotation in a linear magnetic configuration has been investigated by means of high-resolution Doppler-spectroscopy. The effects of external device parameters and ion mass as well as the radial profiles have been studied. A simple model, based on the conservation of the total angular momentum, explains the main empirically determined dependences of the average angular velocity. The results are compared with the common multifluid description developed for hollow cathode discharges.

PACS number(s): 52.90.+z, 52.70.Kz, 52.30.−q

I. INTRODUCTION

Rotation of magnetized plasmas is one of its fundamental and long-known properties. It can be observed in many laboratory plasmas, especially in linear devices like hollow cathodes and is also a common phenomenon in the plasma generator PSI-1 operated at IPP-Berlin. In recent years, the plasma rotation became more and more important, due to its relevance for the confinement in fusion research [1–6]. The so called L-H-transition from the low-confining *L*-mode to the high-confining *H*-mode is caused by a sheared poloidal rotation of the plasma [1,2,6]. Though much work was done in this field [7–19], the origin of the rotation is not yet completely understood.

With respect to isotope separation plasma rotation was mainly investigated between the electrodes of hollow cathode discharges [9,10,12]. The plasma parameters achieved in these devices are very similar to those observed in the PSI-1-facility [19], which is described in Sec. II. The plasma in hollow cathode discharges rotates typically in a right-handed sense with respect to the magnetic field. Its angular velocity is in the range of the ion cyclotron frequency. However, in the vicinity of the anode usually the direction of the rotation changes [20].

The PSI-1 differs in two important aspects from hollow cathode facilities. On the one hand, the electrode geometry is designed to prevent radial currents. On the other hand, the plasma consists of two physically different regions: the source region between cathode and anode and the extended flow region behind the anode. Apart from the diamagnetic current, the latter is current free. In both regions a right-handed rotation is observed. Therefore, two questions arise: First, what is the origin of the radial current needed to sustain the rotation? Second, why does the plasma rotate in the current-free flow region?

The difficulties in describing plasma rotation arise from the fact that radial forces F_r in an axial magnetic field lead to an azimuthal velocity $u_\theta \propto F_r/B_z$ inverse proportional to B_z, i.e., decreasing with increasing magnetic field strength, unless F_r does not depend strongly on B_z itself. In contrast, however, measurements are showing typically $u_\theta \propto B_z$. Hence, for applying the commonly used picture of an $\vec{E}\times\vec{B}$-drift yielding $u_\theta \propto E_r/B_z$ one has to demand $E_r \propto B_z^2$.

On the other hand, starting from the balance of the total angular momentum reasonable results can be achieved, if a driving radial current is assumed. Such current, however, can not be present in plasmas governed by a force balance of the form $\vec{j}\times\vec{B}=\nabla p$ because of $\vec{j}\cdot\nabla p=0$. Therefore, additional forces providing a conductivity $\sigma_\perp$ in radial direction are necessary. Especially viscosity and ion-neutral friction forces have to be taken into account [14,18,21]. Note that in highly ionized plasmas the well-known relation $\sigma_\perp \approx \sigma_\parallel/2$ is meant as the conductivity within the surfaces of constant magnetic flux but not perpendicular to them as needed here.

Viscous forces were proposed by Janssen [11] to explain the radial conductivity. In his widely accepted model he described plasma rotation in hollow cathode discharges invoking the multifluid equations [22,23]. According to this model, the rotation is driven by the Lorentz force due to the radial component of the discharge current. This external torque is finally balanced by ion viscosity. Note that this model is not applicable for a rigid-body rotation as viscosity vanishes in this case.

Although the Janssen model is able to describe hollow cathode experiments it fails to explain the rotation in our case. We rather think that ion-neutral collisions are more important with respect to rotation by affecting the plasma in two ways: On the one hand, the ion transport due to collisions with neutrals provides a radial current and on the other hand the rotation is damped by charge exchange, ionization, and ion neutral friction.

In what follows, we present an overview of the observations related to plasma rotation in the PSI-1 facility. Furthermore, the physical aspects of this phenomenon will be discussed on the basis of a simple balance of the total angular momentum. Although this simple model reflects the main characteristics of the average angular ion velocity Ω_i it is too coarse to describe the radial profiles. For this purpose, further attention has to be put on the processes within the hollow anode where enhanced ion orbit losses may occur due to their large gyro radii.

For the heavy ions the gyro radius can reach the range of the anode diameter ($r_{A,\min}=0.024$ m). Hence, energetic ions

*Present address: UKAEA Fusion, Culham Science Center, Abingdon, Oxon, OX14 3DB, U.K.
†Present address: Institut für Niedertemperaturplasmaphysik, Friedrich-Ludwig-Jahn-Str. 19, D-17489 Greifswald, Germany.

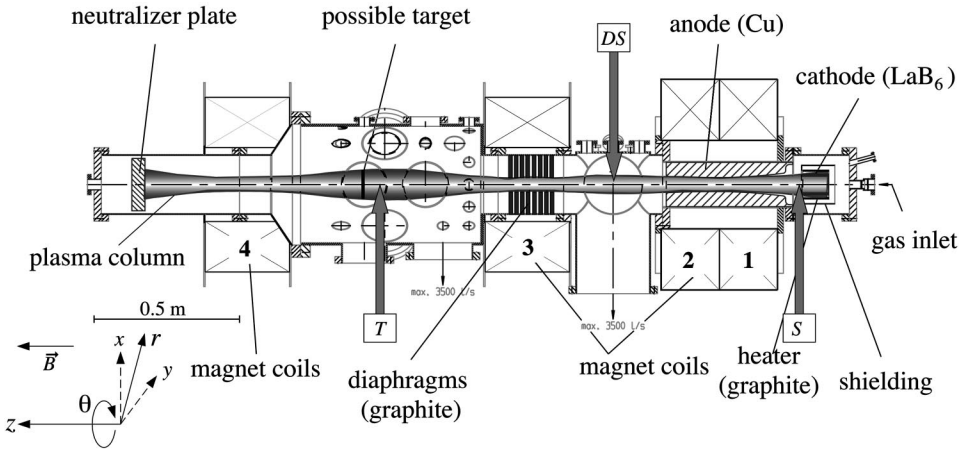

FIG. 1. Schematic view of the PSI-1 device (see also Fig. 14).

can hit the anode surface within one gyro motion whereas the electrons are very tightly bound to the field lines. As a consequence, a radial electric field builds up to confine the ions thereby preventing a continuous charging of the plasma. This mechanism is similar to those proposed to explain the L-H transition in Tokamaks [3,4].

II. EXPERIMENTAL SETUP

The PSI-1 device is schematically shown in Fig. 1. On the right-hand side the source region (S) between anode and cathode is shown where most of the plasma is produced. The adjoining flow region is divided into two chambers: the differential pumping stage (DS) and the target chamber (T). A stationary plasma is generated by the high current ($50\cdots1000$ A) flowing between the hollow cylindrical lanthanum hexa-boride (LaB_6) cathode and the copper hollow-anode. Operating in a low-pressure regime ($0.5\cdots3$ Pa) no self-sustaining discharge can be achieved. Hence, to provide a sufficient electron emission current the cathode is externally heated ($T_c \approx 1900$ K). The voltage between the electrodes is in the range of $10\cdots50$ V. A simple model of the plasma generation is given in Ref. [24]. Confined by a superimposed axial magnetic field B ($0.05\cdots0.25$ T) the plasma is guided through the differential pumping stage into the target chamber where it is neutralized at a conducting end plate. This plasma dump is isolated from the facility and thus at floating potential.

A very powerful diagnostic to measure plasma rotation is the high-resolution (Doppler) spectroscopy (HIRES). A sketch of the experimental set up used in our analysis is shown in Fig. 2. To achieve a resolution as high as $\lambda/\Delta\lambda \approx 3.2\times10^5$ at $\lambda_0 = 434.8$ nm a $f = 1.5$ m spectrometer in Fastie-Ebert mounting and double-pass configuration ($f_{\text{eff}} = 3$ m) is used. A holographic echelle grating with 316 groves/mm at high orders ($k = 8\cdots15$) serves as disperser. The light is predispersed by a Czerny-Turner prism monochromator to subdue effects of lower orders. A plano-convex lens [$f_L = (98.4 \pm 0.4)$ mm] maps the plasma column onto a fiber ($d_{\text{fiber}} = 0.4$ mm), which guides the light to the monochromator system. The lens in front of the entrance slit of the monochromator system adapts the angle of aperture of the fiber and the pre-monochromator. An intensified charge coupled device (CCD) imaging system is used as detector. The spectra are normally magnified by a factor of six to match with the spatial resolution of the CCD chip.

Measurements were performed at three different axial locations as indicated by the big arrows in Fig. 1. In principle, the spectral line intensity I_λ provides three quantities of the observed atom or ion species α: the emissivity ϵ_α, the ve-

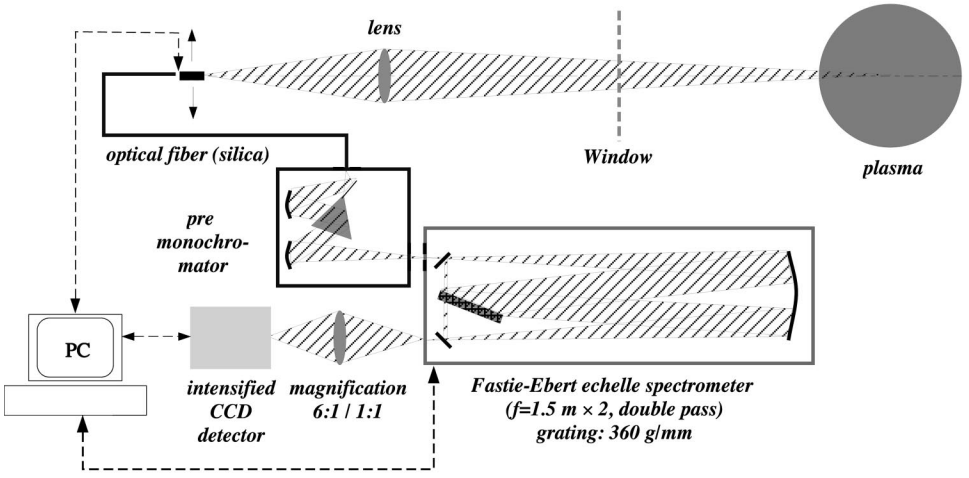

FIG. 2. Experimental setup of the high-resolution spectroscopy (HIRES).

TABLE I. Observed transitions.

		Configuration	Energy		Landé g factor	
	λ_0 [nm]	lower upper	E_l [eV]	E_u [eV]	$g_J^{(l)}$	$g_J^{(u)}$
H_β	486.133	$2p\,^2P^o \leftarrow 4d\,^2D$	10.20	12.75		
H_α	656.279	$2p\,^2P^o \leftarrow 3d\,^2D$	10.20	12.09		
D_β	486.003	$2p\,^2P^o \leftarrow 4d\,^2D$	10.20	12.75		
D_α	656.103	$2p\,^2P^o \leftarrow 3d\,^2D$	10.20	12.09		
He II	468.568	$3d\,^2D_{5/2,3/2} \leftarrow 4f\,^2F^o_{7/2,5/2}$	48.37	51.02		
Ne I	585.283	$3s'[1/2]^o_1 \leftarrow 3p'[1/2]_0$	16.85	18.96	1.03	0
Ne II	366.407	$3s\,^4P_{5/2} \leftarrow 3p\,^4P^o_{3/2}$	27.17	30.55	1.66	1.87
Ar II	434.806	$4s\,^4P_{5/2} \leftarrow 4p\,^4D^o_{7/2}$	16.64	19.50	1.66	1.49
	460.956	$4s'\,^2D_{5/2} \leftarrow 4p'\,^2F^o_{7/2}$	18.46	21.14	1.31	1.24
	611.492	$3d'\,^2G_{9/2} \leftarrow 4p'\,^2F^o_{7/2}$	19.12	21.14	1.19	1.24
Ar III	328.615	$4s\,^5S^o_2 \leftarrow 4p\,^5P_3$	21.62	25.39	2.0	1.71
Kr II	435.547	$5s\,^4P_{5/2} \leftarrow 5p\,^4D^o_{7/2}$	13.99	16.83	1.66	1.49
Kr III	324.569	$5s\,^5S^o_2 \leftarrow 5p\,^5P_3$	18.07	21.88	2.0	1.71
Xe II	484.433	$6s\,^4P_{5/2} \leftarrow 6p\,^4D^o_{7/2}$	11.54	14.10	1.66	1.49

locity u_α and the temperature T_α. The major problem in determining these quantities is the integration over the line of sight which is unavoidable in passive emission spectroscopy. To obtain the spatial (radial) resolution a tomographic reconstruction method is needed. For nonrotating, cylindrical plasmas a simple Abel inversion can be used. For rapidly rotating plasmas with a high azimuthal velocity this normal Abel-inversion fails [12,25]. To handle these difficulties we developed a special Abel-inversion procedure for a plasma rotating with arbitrary velocity [25]. This method enables us to calculate radial profiles of the emissivity $\epsilon_\alpha(r)$, the angular velocity $\Omega_\alpha(r)=u_{\alpha\theta}(r)/r$, and the temperature $T_\alpha(r)$ from the line integrated spectral intensities $I_\lambda(x)$ measured along the whole diameter of the emitting plasma column.

In hydrogen and deuterium, the ions are not directly accessible to optical emission spectroscopy. Even though, we were able to deduce the ion parameters from the neutral line emission by analyzing a part of the Balmer-α and -β emission originating from symmetric charge exchange ($H+H^+ \rightarrow H^+ + H$).

To obtain the correct temperature from the Doppler broadening of the spectral line profiles other mechanisms contributing to the line widths like Stark broadening, the apparatus profile, and the Zeeman effect have to be considered [26]. We include the Zeeman effect and the apparatus function by deconvolution with an effective profile obtained by folding the measured apparatus profile ($\Delta\lambda_{\mathrm{FWHM}} \approx 1.4$ pm) with the Zeeman components of the observed transition. Stark broadening ($\Delta\lambda_{\mathrm{FWHM}} \approx 10^{-3}\cdots10^{-2}$ pm) [27] is negligible compared with the apparatus width. After deconvolution the effective resolution is increased to $\lambda/\Delta\lambda \approx 7.6\times10^5$ [19]. The observed transitions for the various species are tabulated in Table I. Also given are the configuration, the energy and the Landé g-factor for the lower and upper levels of the transition.

III. EXPERIMENTAL RESULTS

In all observable regions, the ions in the PSI-1 show a right-handed rotation with respect to $\vec{B}$. Hence, if $\vec{B}$ points in the z direction the azimuthal velocity $u_{i\theta}$ in a cylindrical system (r,θ,z) is positive (Fig. 1). This is opposite to the direction to the ion diamagnetic drift caused by a negative pressure gradient, which in any case is present at the plasma edge. The angular velocity Ω_i is comparable to the ion cyclotron frequency. In most cases, $\Omega_i \approx 0.4\,\omega_{ci}$ holds. The rotation frequency $f_{rot}=\Omega_i/(2\pi)$ is typically several kHz.

In Fig. 3, the result of a typical measurement of the spectral line intensity of Ar II ($\lambda_0=434.8$ nm) along the plasma diameter is shown as a contour plot. It demonstrates that the Doppler shift due to the azimuthal velocity at the plasma edge is in the same range as the spectral line width. Therefore, the plasma reaches at the edge azimuthal Mach numbers of $M_\theta=0.2\cdots0.8$. Here, the azimuthal Mach number $M_\theta=u_{\alpha\theta}/v_{\mathrm{th},\alpha}$ ($v_{\mathrm{th},\alpha}=\sqrt{2k_B T_\alpha/m_\alpha}$) is defined with respect to the thermal velocity to indicate the importance of inertial forces.

We notice in Fig. 3 a slightly higher intensity at the upper edge compared to the lower one. This asymmetry is caused by an asymmetric power input possibly due to a small axial

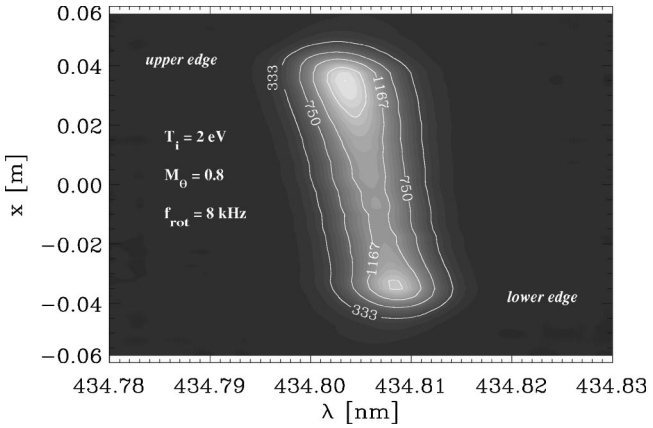

FIG. 3. Typical contour plot of the spectral line intensity of Ar II ($\lambda_0=434.8$ nm) along the plasma diameter (parameters attached to the contours are the counts per exposure time). The wavelength shift at the edge due to the Doppler effect is in the range of the line width.

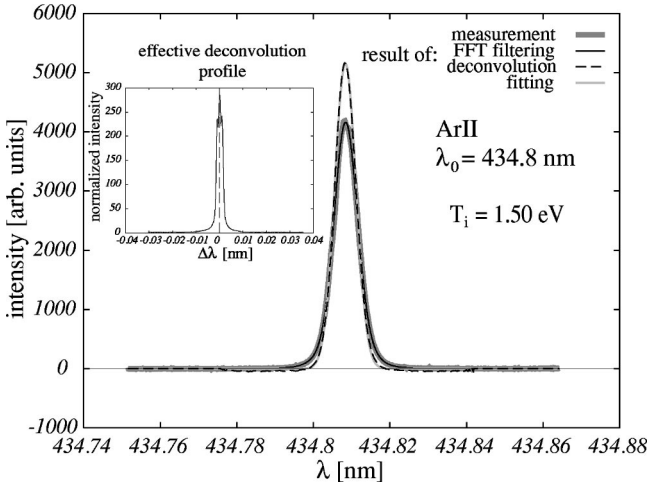

FIG. 4. Typical spectral line intensity profile of Ar II ($\lambda_0 = 434.8$ nm). The results of the different analysis steps (FFT-filtering, deconvolution and fitting) as well as the effective deconvolution profile are shown.

misalignment between the cathode and anode. Therefore, the electron temperature profile is also asymmetric and consequently the intensity profile. To eliminate this effect from the Abel-inversion procedure the intensity profiles are first averaged over the top and bottom position. Since only half of the measurement (e.g., top or bottom) is necessary the comparison of the results from the separate analysis of each side of the profile can be used to estimate the error due to the asymmetry. However, this error is negligible compared to the one caused by finite velocity resolution.

The deconvoluted line profile is to a good approximation a Gaussian (Doppler) profile, as can be seen from Fig. 4. The results of the different steps of the analysis (FFT-filtering, deconvolution and fitting) as well as the effective deconvolution profile are shown. The measured full width half maximum of $\Delta\lambda_{\mathrm{FWHM}} = 6.51$ pm of the Doppler profile corresponds to an ion temperature of $T_i = 1.50$ eV. The maximum distance of the Zeeman-components is $\Delta\lambda_{Z,\max} = 1.7$ pm. The width of the Lorentzian apparatus profile is $\Delta\lambda_{\mathrm{FWHM}} = 1.36$ pm.

In the following, we will discuss the radial profiles of the angular velocity observed in discharges with different gases, succeeded by the analysis of the influence of the different external parameters. For the latter various Ar discharges have been investigated.

A. Radial profiles of Ω_i in different gases

In Fig. 5, the radial profiles of the normalized angular frequency Ω_i/ω_{ci} of hydrogen (H II) and deuterium (D II) ions in discharges with comparable plasma parameters are shown. Here, $\rho_B(r) = \sqrt{\Phi(r)/\Phi_S}$ is the normalized flux coordinate, where Φ are the surfaces of constant magnetic flux and $\Phi_S = 269.4 \times 10^{-6}$ Wb is the flux through the innermost flux surface that touches the anode. This normalization is necessary because of the axial inhomogeneity of B. It enables us to compare radial profiles at different axial positions. The radial profiles of the ion angular velocity in these discharges are slightly peaked at the plasma edge ($\rho_B \approx 1$).

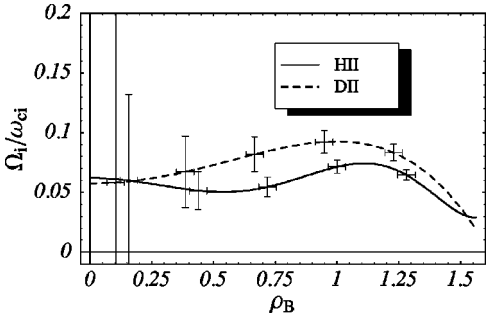

FIG. 5. The radial profile of the normalized angular velocity Ω_i/ω_{ci} of H II and D II in the target chamber for comparable discharge conditions.

As to be seen from Fig. 5, the normalized angular velocity of the ions in hydrogen and deuterium discharges are approximately equal. Hence, the azimuthal velocity is inverse proportional to the ion mass.

To compare the measured angular velocities we would actually have to take the different discharge conditions into account. Thus, only for hydrogen and deuterium, where these are equal a proper comparison is possible. Although the discharge conditions for argon, krypton, and xenon are rather different from those in hydrogen and deuterium, they do not differ markedly amongst each other and a comparison of the normalized ion angular velocity in these gases, as shown in Fig. 6, is reasonable too.

As it can be seen from Fig. 6, also Ar II and Kr II are corroborating the $\Omega_i \propto m_i^{-1}$ dependence, but the rotation of Xe II is about two times faster than expected on this basis. Furthermore, the normalized angular ion velocity in the noble gas plasmas is substantially larger than in the thin hydrogen plasmas, and, in contrast to the radial profiles of H II and D II, those of Ar II, Kr II, and Xe II exhibit no maximum at the plasma edge ($\rho_B \approx 1$).

B. Effects of external parameters on rotation

The discharges are mainly determined by four external parameters. The magnetic flux through the innermost flux surface $\Phi_S = \int_S B_z dS \approx 2\pi r_S^2 B$ ($1.4 \times 10^{-4} \ldots 2.7 \times 10^{-4}$ Wb), the neutral gas pressure within the source region p_s (0.5 . . . 3.0 Pa), the discharge current I_s (50 . . . 600 A), and the voltage U_s (12.7 . . . 46.7 V). Not all of these four parameters can be controlled independently. Note, that the magnetic field strength B on the axis for a given topology varies up to a factor of 5. In the typically used configuration it amounts to $B = 0.05$ T in the target chamber and $B = 0.25$ T inside the coils. In addition, the

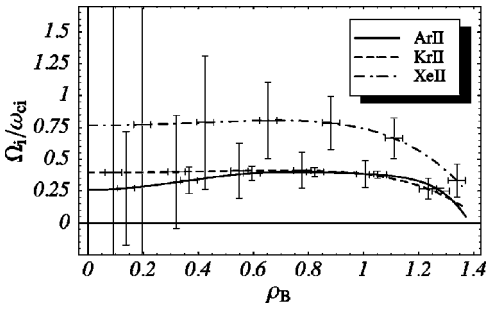

FIG. 6. Same as Fig. 5 for Ar II, Kr II, and Xe II.

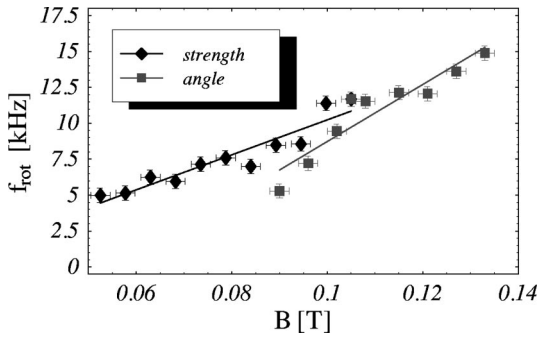

FIG. 7. Effect of the magnetic field on the rotation by changing the strength only (diamonds), and in addition the angle of incidence of the field lines at the anode surface (squares) (I_s, U_s, Q = const).

neutral gas pressure within the target chamber p_t (0.07 . . . 0.38 Pa) can be influential.

The flat profile of the angular velocity (Fig. 6) in argon justifies the characterization of the rotation by a single frequency $f_{\mathrm{rot}}=\Omega_{\mathrm{i}}(\rho_B=1)/2\pi$. Supplementary to the spectroscopic measurements the rotation frequency can be obtained from laser induced fluorescence [28,19] and Fourier transformation of the floating potential of a Langmuir probe [7,19]. The latter one is a more indirect but fast method; it has to be cross checked with the spectroscopic data since the azimuthal modes picked up by the probe may have an additional phase velocity.

The strength and the configuration of the magnetic field at the PSI-1 can be controlled by the current through the two coils (1,2) above the anode and the coil pair (3,4) above the target chamber (Fig. 1). In Fig. 7, the results of two different measurements of the rotation frequency within the differential pumping stage (DS) are shown. In the first case, the strength of the magnetic field was reduced by decreasing the current in all coils to the same fraction (diamonds). In the other case, only the current of the coil number 2 (Fig. 1) above the back part of the anode was varied (squares). This results in a change of the field strength in the vicinity of this coil and simultaneously in a change of the angle of incidence of the magnetic field on the anode as sketched in Fig. 8.

The frequency of the rotation of the plasma rises in both cases linearly with the magnetic field strength. But in the second case (squares) the data can be approximated by a line

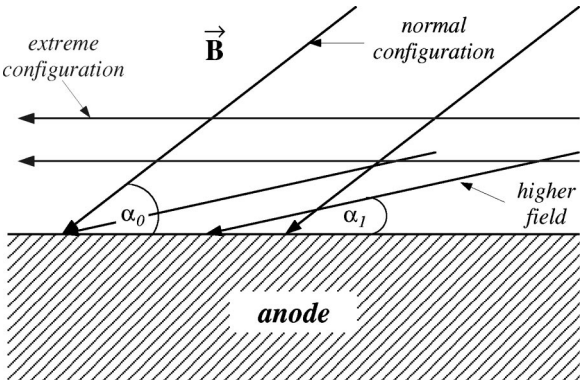

FIG. 8. Sketch of the variation of the angle of incidence of the magnetic field on the anode by changing the current through the coil number 2 above the back part of the anode (Fig. 1).

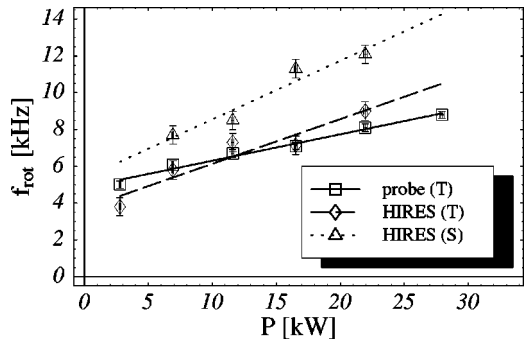

FIG. 9. The rotation frequency in the source region (triangles) and the target chamber (diamonds, squares) increases proportional to the power input ($p_{\mathrm{s}}=1.0$ Pa).

with a steeper slope (Fig. 7). We interpret this observation as follows: A decreasing angle of incidence (α) reduces the projected surface of the anode in the direction of $\vec{B}$. Hence, in order to collect the same total anode current the perpendicular current component $I_\perp=|\vec{B}\times(\vec{I}\times\vec{B})/B^2|=I_{\mathrm{s}}\cos\alpha$ is increased and thus the rotation frequency will be enhanced (see also Sec. IV).

At zero magnetic field strength the rotation frequency should vanish. But the linear approximation of the measurements is of the form $f_{\mathrm{rot}}=c_0+c_1B$. Thus, for small fields this linear law breaks down. Such postulated nonlinear dependence on B was actually found by Boeshoten [10] in a hollow-cathode discharge.

Figures 9–11 show the dependence of the plasma rotation on the discharge conditions. The probe measurements are in good agreement with the spectroscopic results. Both were performed in the target chamber. From Fig. 9, we learn that the rotation frequency in the target chamber and the source region is proportional to the power input. In the source region the plasma is seen to rotate at a substantially higher speed.

To increase the voltage between anode and cathode U_s under constant current I_s the pressure p_s must be decreased. This results in a variation of the well known E/p ratio [29] $[E/p\approx U_s/(Lp_s)]$ which is plotted as abscissa in Fig. 10. The rotation frequency is practically unaffected by this variation. Since a cancellation of the influences of the pressure and voltage is not to be expected, we infer that the rotation is practically independent on the discharge voltage.

Figure 11 shows the variation of f_{rot} with the discharge current I_s for constant discharge voltage U_s. The latter can

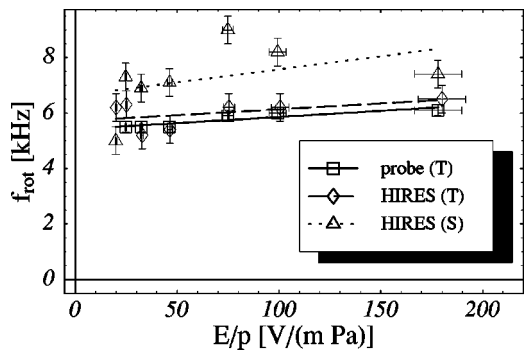

FIG. 10. The E/p ratio, and thus the discharge voltage, has no significant effect on the plasma rotation ($I_{\mathrm{s}}=300$ A).

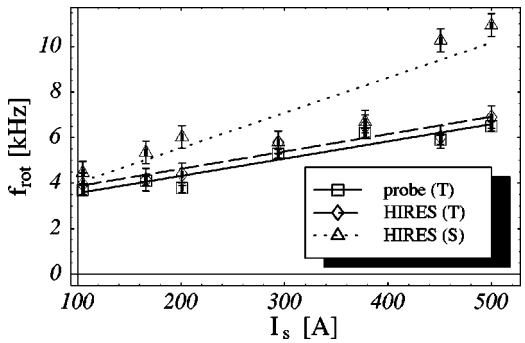

FIG. 11. The rotation frequency in the source region (triangles) and the target chamber (diamonds, squares) is proportional to the discharge current I_s ($U_s = 34.7$ V).

be accomplished by raising the pressure p_s with ascending current. As expected the rotation frequency rises linearly with the current. Again, the rotation velocity is larger in the source region than in the target chamber. The comparison between the results from the target chamber and the source region indicates that the angular momentum of the ions is not constant on magnetic flux surfaces. This loss of angular momentum along the axis is more pronounced at high currents (slope in Fig. 11), i.e., large neutral pressure. These observations are strongly supporting our assumption that the damping of the rotation is caused by the collisions between ions and neutrals. Note, that ion-neutral collisions affect the angular momentum balance in two counteracting ways: On the one hand, the rising neutral density will increase the damping of the rotation. On the other hand, a large neutral density in the source region provides a high perpendicular (Pederson) conductivity and thus a large radial current that drives the rotation.

By collisions of the ions with neutrals, like charge exchange or elastic collisions angular momentum is transferred from the plasma to the walls. Also ionization acts as a sink of angular momentum by producing slow ions that are to be accelerated. Hence, all three processes damp the rotation. This damping is proportional to the characteristic collision frequency $\nu_{i0} = n_0 \langle \sigma_{i0} v_i \rangle$ being proportional to the neutral density. Further evidence for this mechanism is given by the measurements shown in Fig. 12, where only the neutral pressure p_t in the target chamber has been varied. Assuming a

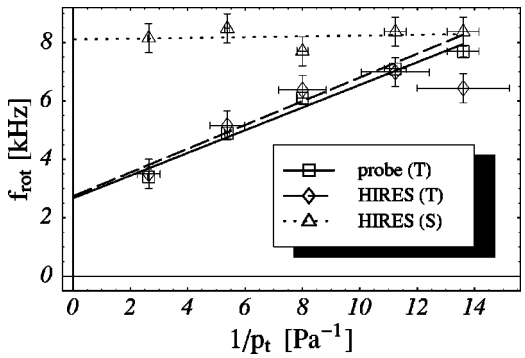

FIG. 12. The rotation frequency in the target chamber (diamonds, squares) is inverse proportional to the local neutral pressure. No change is observed in the source region where the neutral pressure stays constant.

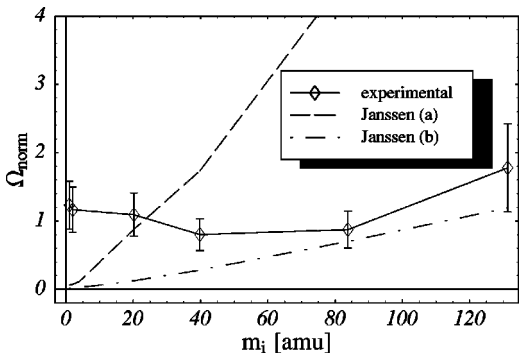

FIG. 13. Angular velocity for various discharge gases normalized by means of Eq. (7). The theoretical results according to Janssen are also shown for two limiting ratios of the electron temperature (a: $T_e^{(s)}/T_e^{(T)} = 1$; b: $T_e^{(s)}/T_e^{(T)} = 4$).

constant temperature for the neutrals, the pressure is proportional to the neutral density and thus inverse proportional to the characteristic collision time $\tau = 1/\nu$. Note that in the source region the rotation does not change. Since here all parameters were kept constant it is inferred that rotational damping is a local process.

C. Summary of the experimental results

To compare the angular velocity of all investigated discharge gases we have normalized Ω_i by means of Eq. (7) given in Sec. IV. The prediction of the theory developed by Janssen [11] is also plotted for comparison. In this theory the electron temperature in the source region $T_e^{(s)}$ enters sensitively through the parallel conductivity. As the electron temperature varies for each gas the uncertainty of our knowledge about T_e inside the source region is covered by showing two curves (*a*, *b*) with the smallest and largest ratios of $T_e^{(s)}/T_e^{(T)} = 1$ and $T_e^{(s)}/T_e^{(T)} = 4$, respectively. Irrespective of the large influence of T_e we notice that the model is unable to describe the mass dependence found in the experiments.

With the exception of Xe II (last point in Fig. 13) the dependence predicted by Eq. (7) agrees well with the measurements. Especially for the heavy Xe ions finite gyro radius effects within the anode could become important. For normalization of the rotation frequencies some unknown quantities have to be estimated, which will be discussed in the next section.

IV. A SIMPLE MODEL

A. Conservation of the total angular momentum

The essential dependences of Ω_i can already be understood by considering the balance of the total angular momentum

$$\vec{L} = m_i \int_{V_p} n_i (\vec{r} \times \vec{u}_i) dV \tag{1}$$

of the rotating plasma. Because of the smallness of the electron mass only the ions have to be taken into account. The plasma continuously loses angular momentum by charge exchange and particle losses at the periphery and, most important, at the neutralizer plate. A constant gas flow (Q) is fed

into the device. Most of the in-flowing neutrals are ionized within the source region and axially transported along the field lines to the limiting walls. Hence, in the stationary case the (damping) torque exerted by the neutrals reads:

$$\vec{M}^{(Q)} = -\frac{m_i Q}{V_p}\int_{V_p} \alpha_{\rm ion}\vec{r}\times\vec{u}_i dV + \int_{V_p}\vec{r}\times\vec{R}_{i0} dV, \qquad (2)$$

where $\alpha_{\rm ion} = n_i/(n_i+n_0)$ denotes the degree of ionization, V_p the plasma volume and $\vec{R}_{i0} = -\mu_{i0} n_i \nu_{i0}\vec{u}_i$ is the neutral friction force density [$\mu_{i0} = m_i m_0/(m_i+m_0) = m_i/2$: reduced mass]. The first integral in Eq. (2) accounts for the loss of ions—under stationary conditions—which are replaced by an equal incoming flux being provided by neutrals that are ionized with the probability $\alpha_{\rm ion}$. The second integral describes the damping due to charge exchange and elastic collisions.

This loss of angular momentum has to be balanced by an external torque due to the $\vec{j}\times\vec{B}$-force integrated over the source region (cathode-anode)

$$\vec{M}^{(I)} = \int_{V_s}\vec{r}\times(\vec{j}\times\vec{B}) dV. \qquad (3)$$

In the stationary case the total angular momentum is constant and the total torque

$$\vec{M} = \vec{M}^{(Q)} + \vec{M}^{(I)} = 0 \qquad (4)$$

must vanish.

Let us assume a cylindrical, axial homogeneous plasma with radius R and length L_p under rigid rotation ($u_{i\theta} = \Omega_i r$). The plasma density shall also be homogeneous in radial direction. Inserting Eqs. (2) and (3) into the axial component of Eq. (4) and integrating over θ and z, we obtain

$$\frac{m_i}{2}\left(n_i\nu_{i0} + \frac{2\alpha_{\rm ion}Q}{V_p}\right) L_p\Omega_i \int_0^R r^3 dr + BL_s\int_0^R r^2 j_r dr = 0, \qquad (5)$$

where L_p and L_s are the lengths of the plasma and the source region, respectively. Hence, a positive rotation can only be achieved with a negative radial current.

In the PSI-1 device, however, this current should exist only in the radial range $R-\delta \leqslant r \leqslant R$. Due to $\nabla\cdot\vec{j} = 0$ the axial current must change. Because of the high parallel conductivity $\sigma_\parallel$, compared to $\sigma_\perp$, we approximate the change of the axial current density by means of the linear ansatz $j_z = -I_s(1-Cz)/[\pi\delta(2R-\delta)]$ (see Sec. IV B). The radial current density is then obtained from $\nabla\cdot\vec{j} = 0$ to

$$j_r = -\frac{I_s C}{2\pi\delta(2R-\delta)}\Theta(r-[R-\delta])\left[r - \frac{(R-\delta)^2}{r}\right], \qquad (6)$$

where $\Theta(r)$ is the unit step (Heaviside) function. Now we are able to perform the integration in Eq. (5). Solving for the angular velocity we obtain

$$\Omega_{\rm i} = C\frac{I_s B}{m_i(V_p n_i\nu_{i0} + 2\alpha_{\rm ion}Q)}\cdot\frac{L_s\delta(2R-\delta)}{R^2}. \qquad (7)$$

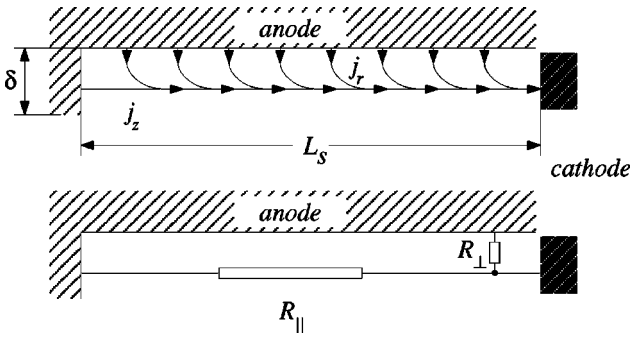

FIG. 14. Sketch of the current flow in the source region (top) and equivalent circuit (bottom).

The collision frequency can be approximated by $\nu_{i0} = n_0(\sigma_{i0}+\sigma_{\rm CX})\overline{v_{\rm i}}$, where $\sigma_{i0}\approx\pi r_g^2$ is the cross section for elastic ion-neutral collisions with $r_g \approx 2r_0$ the gas-kinetic radius, $\sigma_{\rm CX}\approx\sigma_0[1+a\ln(E_0/E)]$ is the cross section for resonant charge exchange and $\overline{v_{\rm i}} = \sqrt{8k_{\rm B}T_{\rm i}/(\pi m_{\rm i})}$ is the mean velocity [$\sigma_0 = \sigma_{\rm CX}(E_0)$ and a are tabulated in Ref. [30]].

B. Evaluation of the current decay coefficient *C*

The last step is to evaluate the constant C. A schematic view of the current flow is shown in Fig. 14. As a first approximation we can use the equivalent circuit also depicted in Fig. 14 and estimate C by means of the junction theorem, which leads to

$$CL_s = \frac{I_\perp}{I_\perp + I_\parallel} = \frac{R_\parallel}{R_\perp + R_\parallel}. \qquad (8)$$

Assuming constant radial and parallel conductivity $\sigma = 1/\eta$ the resistance $R = \int \eta/A\, dl$ can be written as

$$R_\perp = \int_{R-\delta}^{R}\frac{dr}{2\pi r L_s\sigma_\perp} = -\frac{1}{2\pi L_s\sigma_\perp}\ln\frac{R-\delta}{R} \approx \frac{\delta}{2\pi R L_s\sigma_\perp} \qquad (9)$$

$$R_\parallel = \int_0^{L_s}\frac{dz}{\pi\delta(2R-\delta)\sigma_\parallel} = \frac{L_s}{\pi\delta(2R-\delta)\sigma_\parallel}. \qquad (10)$$

Inserting Eqs. (9) and (10) into Eq. (8) we get

$$C = \frac{2RL_s\sigma_\perp}{\delta^2(2R-\delta)\sigma_\parallel + 2RL_s^2\sigma_\perp} \approx \frac{L_s\sigma_\perp}{\delta^2\sigma_\parallel + L_s^2\sigma_\perp}$$

$$= \frac{1}{L_s\left(\dfrac{\delta^2}{L_s^2}\dfrac{\sigma_\parallel}{\sigma_\perp} + 1\right)}, \qquad (11)$$

where the parallel and perpendicular conductivity are to be specified.

The parallel conductivity in a highly ionized plasma is given by Spitzers formula for $Z_{\rm eff} = 1$ (Ref. [31])

$$\sigma_\parallel = 1.96\frac{n_e e^2\tau_{ei}}{m_e} \propto T_e^{3/2}, \qquad (12)$$

which for the case of argon ($n_e = 4.4\times10^{20}$ m^{-3}, $T_e = 5.2$ eV) yields $\sigma_\parallel \approx 3.5\times10^4$ $(\Omega\,\mathrm{m})^{-1}$.

In a fully ionized plasma there is no radial conductivity [31] up to a second order expansion with respect to the ratio of gyro radius to length of pressure gradient. However, inertia effects, viscosity, and collisions with neutrals provide a finite radial conductivity. We want to focus on the latter effect only (though finite gyro radius effects might be important for heavy ions too).

An expression for the radial current density can be derived from the single-fluid momentum balance equation. We start from the momentum balance equation for electrons and ions in a single ionized plasma

$$m_e n_e \frac{d\vec{u}_e}{dt} + \nabla\cdot\boldsymbol{\pi}_e = -\nabla p_e + e n_e(\vec{E} + \vec{u}_e\times\vec{B}) + \vec{R}_e - m_e\vec{u}_e S_e \tag{13}$$

$$m_i n_i \frac{d\vec{u}_i}{dt} + \nabla\cdot\boldsymbol{\pi}_i = -\nabla p_i - e n_i(\vec{E} + \vec{u}_i\times\vec{B}) + \vec{R}_i - m_i\vec{u}_i S_i\,. \tag{14}$$

Here, $\vec{R}_\alpha$ is the friction force, $\boldsymbol{\pi}_\alpha$ is the viscosity tensor, S_α is the source term and $d\vec{u}_\alpha/dt = \partial_t\vec{u}_\alpha + (\vec{u}_\alpha\cdot\nabla)\vec{u}_\alpha$ denotes the substantive derivative of $\vec{u}_\alpha$ $(\alpha = e,i)$. In what follows we neglect the inertia and viscosity terms on the left hand side of Eqs. (13) and (14) and assume quasi-neutrality $n_e = n_i = n$. Adding the two momentum balance equations yields

$$\vec{j}\times\vec{B} = \nabla p - (\vec{R}_e + \vec{R}_i) + m_e\vec{u}_e S_e + m_i\vec{u}_i S_i\,, \tag{15}$$

where $p = p_e + p_i$, the total pressure, and $\vec{j} = en(\vec{u}_i - \vec{u}_e)$, the current density, has been introduced. Note that all elastic electron-ion collisions in Eq. (15) cancel and in essence only collisions with neutrals are left. Assuming a vanishing velocity $\vec{u}_0 = 0$ for the neutrals the remaining part of the friction force and the source terms are of the same form $m_\alpha n\nu\vec{u}_\alpha$ and from the azimuthal component of Eq. (15) we deduce

$$j_r = -\frac{n m_i}{B_z}\left[\nu_i^{\mathrm{eff}} u_{i\,\theta} + \frac{m_e}{m_i}\nu_e^{\mathrm{eff}} u_{e\theta}\right], \tag{16}$$

where $\nu_\alpha^{\mathrm{eff}}$ is the effective collision frequency. For ions

$$\nu_i^{\mathrm{eff}} = \frac{1}{2}\underbrace{(\nu_{i0}^{\mathrm{el}} + \nu_{i0}^{\mathrm{cx}})}_{\nu_{\mathrm{io}}} + \nu_{\mathrm{ion}} \tag{17}$$

is determined by elastic collisions $\nu_{i0}^{\mathrm{el}} \approx n_0\overline{v_i}\sigma_{i0}$, charge exchange $\nu_{i0}^{\mathrm{cx}} = n_0\overline{v_i}\sigma_{CX}$ and ionization $\nu_{\mathrm{ion}} = n_0\langle\sigma_{\mathrm{ion}}v_e\rangle$. The factor 1/2 in Eq. (17) results from the reduced mass, which enters the friction force. For the electrons the effective collision frequency is given by

$$\nu_e^{\mathrm{eff}} = \nu_{e0}^{\mathrm{el}} + \nu_{e0}^{\mathrm{ex}} + \nu_{ei}^{\mathrm{ex}} + \nu_{\mathrm{ion}}\,. \tag{18}$$

Here, besides the elastic collisions and the ionization term also the momentum losses due to excitation of neutrals $\nu_{e0}^{\mathrm{ex}} = n_0\langle\sigma_{e0}^{\mathrm{ex}}v_e\rangle$ and ions $\nu_{ei}^{\mathrm{ex}} = n\langle\sigma_{ei}^{\mathrm{ex}}v_e\rangle$ resulting from the electron source term enter. Generally, the effective collision frequencies for electrons and ions are of the same order of magnitude. As so are the azimuthal velocities. Hence, the second term on the right-hand side of Eq. (16) can be neglected due to the smallness of the electron mass. Using the radial component of Eq. (14), neglecting the small term containing the radial velocity we find

$$u_{i\theta} = \frac{1}{enB_z}\frac{\partial p_i}{\partial r} - \frac{E_r}{B_z}$$

and thus

$$j_r = \frac{n m_i \nu_i^{\mathrm{eff}}}{B_z^2}\left(E_r - \frac{1}{en}\frac{\partial p_i}{\partial r}\right) = \sigma_\perp\left(E_r - \frac{1}{en}\frac{\partial p_i}{\partial r}\right), \tag{19}$$

where the factor

$$\sigma_\perp = m_i n\nu_i^{\mathrm{eff}}/B_z^2 \tag{20}$$

is the radial conductivity [32]. Together with Eq. (12) this yields for the ratio of conductivities

$$\frac{\sigma_\perp}{\sigma_\parallel} = 0.51\frac{\nu_{ie}\left(\nu_{\mathrm{ion}} + \frac{1}{2}\nu_{i0}\right)}{\omega_{ce}\omega_{ci}}, \tag{21}$$

where ν_{ie} is the electron ion collision frequency. Again, for argon discharges ($T_i = 1.5$ eV, $n_0 = 2.4\times10^{19}$ m^{-3}, $\sigma_{CX} \approx 4.5\times10^{-19}$ m^2, $\sigma_{i0} \approx 0.9\times10^{-19}$ m^2, $\langle\sigma_{\mathrm{ion}}v_e\rangle = 2.8\times10^{-15}$ m^3/s, and the other parameters as for the calculation of $\sigma_\parallel$) we obtain this time $\sigma_\perp \approx 120$ $(\Omega\,\mathrm{m})^{-1}$ and with the previous result a ratio of $\sigma_\perp/\sigma_\parallel \approx 3.5\times10^{-3}$.

Now, we are able to calculate the theoretical angular velocities from Eq. (7) using Eqs. (11), (12), and (20). For the unknown quantities inside the anode, like δ, n_0, T_e, and $n_e = n_i$, reasonable values have to be chosen. For an oblique magnetic field with respect to the conducting surface as in our case a magnetic presheat develops, which is in the range of the ion gyro radius $\rho_i = v_{\mathrm{th,i}}/\omega_{ci}$ [33]. Thus, $\delta \approx \rho_i$ is a reasonable choice. The neutral density was calculated from the measured neutral pressure in the source region by assuming a temperature of $T_0 = 3000$ K, which is the typical temperature measured spectroscopically in Ne and Ar. Except for hydrogen and deuterium, where $T_0 = 2$ eV is assumed due to molecule dissociation. Electrons are treated as isothermal and the measured value in the target chamber given in Table II (see Fig. 1) is inserted into Eq. (7). According to results in argon [19] the electron density measured in the target chamber is enhanced by a factor of seven to approximate n_e inside the anode.

TABLE II. Electron temperatures in the target chamber.

	H_2	D_2	Ne	Ar	Kr	Xe
T_e [eV]	5	5	6	2	2	2

The good agreement with Eq. (7) can also be seen from Fig. 15, which shows the measured angular velocities of Ar II for different discharge currents (see also Fig. 11) compared to the calculated values by means of Eq. (7). Here, the following typical parameters inside the source region are used:

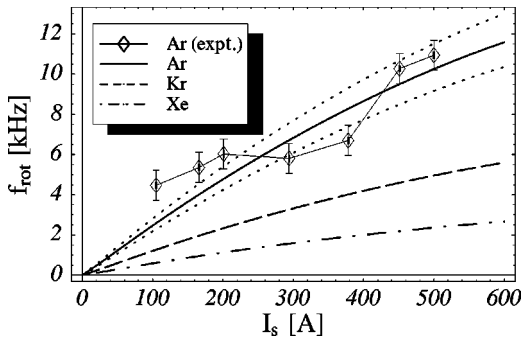

FIG. 15. Current dependence of f_{rot} by means of Eq. (7) for Ar, Kr, and Xe. The dotted lines mark the effect of a 10% variation in T_e.

$L_s=0.47$ m, $R=0.028$ m, $\delta=\rho_{\mathrm{i}}=\sqrt{2m_ik_BT_i}/(eB)$, $B=0.14$ T, $T_i^{\dagger}=1.3(I_s/I_0)+0.18(I_s/I_0)^2$ eV, $T_e=5.2$ eV, $n_{\mathrm{e}}^{\dagger}=n_{\mathrm{i}}=4.4\times10^{20}(I_s/I_0)^{1/3}$ m^{-3} ($I_0=150$ A), $n_0=2.4\times10^{19}$ m^{-3}, and $Q^{\dagger}=2.4\times10^{19}$ particles/s. The quantities marked with a dagger are chosen to match those relevant for the experimental data set shown in Fig. 15. The nonlinear behavior results from the current dependence of the electron (ion) density [19,24]. Although this estimation describes the empirically obtained dependencies quite satisfactorily for a more detailed analysis profile effects would have to be taken into account and in addition finite gyro-radii effects may become relevant in some cases.

V. CONCLUSION

We have investigated the plasma rotation within a large range of parameters. In particular, the mass dependence of the rotation was studied, which allows a critical test on various theories.

The plasma ions rotate in the opposite direction to their diamagnetic drift, i.e., right handed with respect to $\vec{B}$. The azimuthal velocity at the plasma edge reaches Mach numbers of 0.2 to 0.8. For discharges in heavy noble gases the rotation— apart from the plasma edge—is almost free of shear. For lighter gases, a maximum in the angular velocity at the plasma edge due to a hollow ion pressure profile develops.

In general, the rotation behavior in our PSI-1 device resembles the observations made in hollow cathode discharges [7–12]. The viscosity model, however, generally evoked for interpretation [11], fails to describe our results. Within the investigated parameter range the results are in good agreement with Eq. (7), derived from a balance of the total angular momentum. Here, the ion neutral collisions are essential. These collisions provide the plasma with a small perpendicular electrical conductivity needed to sustain a radial current. Simultaneously the same collisions damp the rotation by transporting angular momentum out of the plasma volume. The angular momentum produced in the source region between cathode and anode is transported into the current-free extended flow region beyond the anode along $\vec{B}$. The damping within this region is observable but quite small because of the low neutral density.

ACKNOWLEDGMENTS

The authors would like to acknowledge fruitful discussions with H. Kastelewicz, M. Laux, D. Naujoks, U. Wenzel, and M. Brix. We would also like to thank the PSI-1 Team for support in performing the experiments.

[1] R.J. Taylor, M.L. Brown, B.D. Fried, H. Grote, J.R. Liberati, G.J. Morales, P. Pribyl, D. Darrow, and M. Ono, Phys. Rev. Lett. **63**, 2365 (1989).
[2] R.J. Taylor, R.W. Conn, B.D. Fried, R.D. Lehmer, J.R. Liberati, P.A. Pribyl, L. Schmitz, G.R. Tynan, B.C. Wells, D.S. Darrow, and M. Ono, in *Proceedings of the 13th International Conference on Plasma Physics and Controlled Fusion Research, Washington, D.C., 1990*, edited by J. Weie and M. Spak (International Atomic Energy Agency (IAEA), Vienna, 1991), Vol. 1.
[3] K.C. Shaing and E.C. Crume, Jr. Phys. Rev. Lett. **63**, 2369 (1989).
[4] K.C. Shaing, E.C. Crume, Jr., and W.A. Houlberg, Phys. Fluids B **2**, 1492 (1990).
[5] J.N. Talmadge, B.A. Peterson, D.T. Anderson, F.S.B. Anderson, H. Dahi, J.L. Shohet, M. Coronado, K.C. Shaing, M. Yokoyama, and M. Wakatani, in *Proceedings of the 15th International Conference on Plasma Physics and Controlled Nuclear Fusion Research, Seville, Spain, 1994*, edited by J. Weie and M. Spak (International Atomic Energy Agency (IAEA), Vienna, 1995), Vol. 1.
[6] ASDEX-Team, Nucl. Fusion **29**, 1959 (1989).
[7] D.L. Morse, Phys. Fluids **8**, 516 (1965).
[8] C.B. Kretschmer, F. Boeschoten, and L.J. Demeter, Phys. Fluids **11**, 1050 (1968).
[9] J.L. Delcroix and A.R. Trindade, in *Advances in Electronics and Electron Physics* (Academic Press, New York, 1974), Vol. 34.
[10] F. Boeschoten, R. Komen, and A.F.C. Sens, Z. Naturforsch. A **34a**, 1009 (1979).
[11] P.A.E.M. Janssen and F.J.F. Odenhoven, Physica C **98**, 113 (1979).
[12] M. Bessenrodt-Weberpals, E.K. Souw, J. Uhlenbusch, and H. Kempkens, Plasma Phys. Controlled Fusion **26**, 409 (1984).
[13] V. Rozhansky and M. Tendler, Phys. Fluids B **4**, 1877 (1992).
[14] M. Coronado and J.N. Talmadge, Phys. Fluids B **5**, 1200 (1992).
[15] H. Xiao, R.D. Hazeltine, and P.M. Valanju, Phys. Plasmas **1**, 3641 (1994).
[16] H. Wobig, Plasma Phys. Controlled Fusion **38**, 1053 (1996).
[17] S.N. Arteha, Phys. Plasmas **3**, 2849 (1996).
[18] A.G. Peeters, Phys. Plasmas **5**, 763 (1998).
[19] H. Meyer, Ph.D. thesis, Humboldt-Universität zu Berlin, 1998.
[20] V.M. Lelevkin, D.K. Ortorbaev, and D.C. Schram, *Physics of Non-Equilibrium Plasmas* (North-Holland, Amsterdam, 1992).
[21] E.R. Solano and R.D. Hazeltine, Phys. Fluids B **2**, 2113 (1990).
[22] A. Schlüter, Z. Naturforsch. **5** A(2), 72 (1950).
[23] S.I. Braginskii, in *Review Plasma Physics* (Consultants Bu-

reau, New York, 1966), Vol. 1.
[24] D. Naujoks, G. Fussmann, and H. Meyer, Contrib. Plasma Phys. **38**, 127 (1998).
[25] G. Fussmann, H. Meyer, and E. Pasch, Contrib. Plasma Phys. **36**, 501 (1996).
[26] H.R. Griem, *Plasma Spectroscopy* (McGraw-Hill, New York, 1964).
[27] H.R. Griem, *Spectral Line Broadening by Plasmas*, Pure and Applied Physics Vol. 39 (Academic Press, New York, 1974).
[28] M.J. Goeckner and J. Goree, J. Vac. Sci. Technol. A **7**, 977 (1989).
[29] *Elektroden-Emission und Gasentladungen I*, edited by S. Flügge, Handbuch der Physik Vol. 21 (Springer Verlag, Berlin, 1956).
[30] A. Anders, *A Formulary for Plasma Physics* (Akademie-Verlag, Berlin, 1990).
[31] L. Spitzer, Jr., *Physics of Fully Ionized Gases* (Interscience, London, 1956).
[32] D.L. Winslow, R.D. Bengston, B. Richards, and A.J. Wootton, Phys. Plasmas **5**, 752 (1998).
[33] R. Chodura, *Physics of Plasma Wall Interaction in Controlled Fusion*, Vol. 131 of *NATO Advanced Studies Institute Series, Series B: Physics*, edited by D.E. Post and R. Behrish (Plenum Press, New York, 1984).